

ILD benchmark analysis on WIMP

Ryo Yonamine¹

¹Department of Physics, Tohoku University, Sendai 980-8578, Japan

September 2019

Abstract

Weakly interacting massive particles (WIMPs) have been considered as attractive candidates for dark matter that are expected to exist based on a variety of astronomical observations. The ILC is expected to play a key role to search for WIMPs and investigate their properties with EFT, which can describe the process almost model-independently. This study aims for examining the detector and physics performances for two different ILD detector models namely IDR-L and IDR-S. We found the physics performances for these two models were almost identical.

1 Introduction

The International Linear Collider (ILC) is expected to play a key role in a search for Weakly Interacting Massive Particles (WIMPs) as compelling candidates of dark matter, which are expected from many astrophysical and cosmological observations, and their interpretation within the Λ CDM model. The main target process considered at the ILC is WIMP pair-production, where the interaction is tagged by observing a hard ISR photon and no other activity in the detector. The process of WIMP pair-production at the ILC can be described in an almost model-independent way using the Effective Field Theory (EFT) approach.

In the EFT approach, the process is treated as an effective four-point interaction ($\frac{g_f g_\chi}{q^2 - M^2} \rightarrow \frac{1}{\Lambda^2}$) instead of looking at many free parameters of a particular model (mediator mass (M) and couplings (g_f, g_χ)). This means we presumed the mass of the mediator particle to be well above the maximum momentum transfer scale given by \sqrt{s} .

We examined the detector and physics performances for two different ILD detector models namely IDR-L and IDR-S, which differ in detector radius (IDR-L: ~ 7.7 m, IDR-S: ~ 7.4 m) and in the strength of the magnetic field (IDR-L: 3.5 T, IDR-S: 4 T). We naively expected no significant difference for this analysis where ISR photons are the only observables, but there may be some visible effect due to different magnetic fields. This study is based on the earlier study done by M. Habermehl [1]. The analysis code used in this paper is available at [2].

This note is organized as follows: In Sec. 2, we describe our analysis setup, and how we select the signal events. In Sec. 3, we briefly summarize our simulation setup and generated MC samples. In Sec. 4 and 5, we discuss event selection performance and physics performance, respectively. Finally Sec. 6 gives our conclusion.

2 Analysis setup and MC samples

2.1 WIMP Signal and background

To study the WIMP discovery reach, ISR photon energy spectra for signal and background were produced. Instead of repeating a full chain of the event generation and reconstruction for several WIMP hypotheses, we made use of the $e^+e^- \rightarrow \nu\nu + \text{ISR}$ events, which contribute to the irreducible background to WIMP pair-production process. We define WIMP signal event samples by reweighting a half of the $e^+e^- \rightarrow \nu\nu + \text{ISR}$ event samples, with weight functions depending on the polar angle (θ_γ) and the energy (E_γ) of the ISR photon. Figure 1 shows an example of reweighting the photon energy distribution from $e^+e^- \rightarrow \nu\nu + \text{ISR}$ events assuming a WIMP mass of 10 GeV, beam polarization of -80% for the electrons and +30% for the positrons and an integrated luminosity of 500fb^{-1} . The other half of the $e^+e^- \rightarrow \nu\nu + \text{ISR}$ event samples are used as background.

Apart from the $e^+e^- \rightarrow \nu\nu + \text{ISR}$ background mentioned above, also the Bhabha process ($e^+e^- \rightarrow e^+e^- + \text{ISR/FSR}$) gives significant background contribution because the electrons are often scattered at too small angles to detect. Other Standard Model processes, which could be considered as a background, either contain jets or charged particles, which makes it relatively easy to distinguish them from a WIMP pair-production event. At the earlier studies [3, 4] they were shown to give a small contribution to the final background level. As this study focuses on the detector performance effects, processes other than $e^+e^- \rightarrow \nu\nu$ and $e^+e^- \rightarrow e^+e^- (+ \text{ISR})$ are not considered.

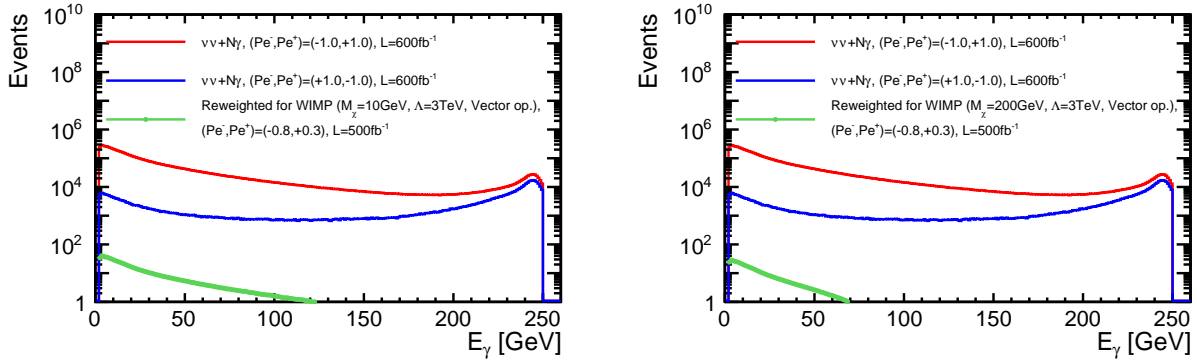


Figure 1: Examples of reweighting photon energy distribution from $e^+e^- \rightarrow \nu\nu + \text{ISR}$ events assuming a WIMP mass of 10 GeV (left) and a WIMP mass of 200 GeV (right). An energy scale (Λ) of 3 TeV, the vector type coupling, the beam polarization of -80% for electron and +30% for positron and the integrated luminosity of 500fb^{-1} are assumed for these examples.

2.2 Simulation setup

The event samples used in this study were generated using WHIZARD version 2.4.4 [5, 6] followed by detector simulation and event reconstruction using standard ILD tools based on DD4hep [7] and MarlinReco [8]. The phase space region for one of the ISR photons was adjusted to almost the signal definition at the event generation to save CPU time. We needed additional cuts to avoid a divergence of the cross-section for the events containing more than one photon. A detailed description can be found in Section 5.3.2 in [1].

The cross sections and the number of generated events of the MC samples used in this report are summarized in the Tab. 1. Detailed information of the MC samples used in this study can be found at the links listed in the Tab. 2.

process	(e pol., e^+ pol.)	$\sigma[fb]$	N events	corr. luminosity [fb^{-1}]	
$\nu\nu N\gamma$	(-1,+1)	28093.1	32.7	16855886	600.0
	(+1,-1)	1937.6	2.7	1162572	600.0
$eeN\gamma$	(-1,-1)	123911.1	72.4	3000009	24.21
	(-1,+1)	133070.8	78.4	3000009	22.54
	(+1,-1)	130234.7	75.2	3000009	23.04
	(+1,+1)	123916.5	70.1	3000009	24.21

Table 1: The cross sections and the number of generated events for the MC samples used in this note.

Model	process	(e pol., e^+ pol.)	URL
IDR-L	$\nu\nu N\gamma$	(-1,+1)	https://ild.ngt.ndu.ac.jp/eelog/dbd-prod/240
		(+1,-1)	https://ild.ngt.ndu.ac.jp/eelog/dbd-prod/240
	$eeN\gamma$	(-1,-1)	https://ild.ngt.ndu.ac.jp/eelog/dbd-prod/241
		(-1,+1)	https://ild.ngt.ndu.ac.jp/eelog/dbd-prod/242
		(+1,-1)	https://ild.ngt.ndu.ac.jp/eelog/dbd-prod/243
		(+1,+1)	https://ild.ngt.ndu.ac.jp/eelog/dbd-prod/246
IDR-S	$\nu\nu N\gamma$	(-1,+1)	https://ild.ngt.ndu.ac.jp/eelog/dbd-prod/287
		(+1,-1)	https://ild.ngt.ndu.ac.jp/eelog/dbd-prod/287
	$eeN\gamma$	(-1,-1)	https://ild.ngt.ndu.ac.jp/eelog/dbd-prod/283
		(-1,+1)	https://ild.ngt.ndu.ac.jp/eelog/dbd-prod/284
		(+1,-1)	https://ild.ngt.ndu.ac.jp/eelog/dbd-prod/285
		(+1,+1)	https://ild.ngt.ndu.ac.jp/eelog/dbd-prod/286

Table 2: MC samples used in this note. There is another set of s5 samples also in the links listed as IDR-L category (240-246) but we did not use them due to the fact that they were produced with a wrong BCal background map.

3 Event selection

We select our signal events taking into account reconstruction deficits and features of the detector, and avoid regions in parameter space with high background levels. WIMP signal events, in principle, have only a single photon and contain no charged particles. We, however, expect charged particles from beam-induced photon-photon interactions even for such signal events. Hence, requirements for the transverse momentum (p_T), the visible energy (E), and the number of clusters in a very forward region (BCal) with considering the beam background play a key role to suppress SM processes.

3.1 Requirements for signal photon candidates

cos θ First, we require the photon to be within tracker acceptance to distinguish photons and charged particles. An efficient track reconstruction with the Forward Tracking Disks is possible above 7° . This leads to our requirement for the polar angle of $7^\circ < \theta < 173^\circ$.

p_T Second, we require a minimum transverse momentum of the photon so that we can identify Bhabha events, which requires that at least one electron or positron in each Bhabha event is reconstructed in the detector. This ensures to suppress the Bhabha scattering background. Since the inner rim of BeamCal has a ϕ -dependent shape, we apply the p_T cut depending on ϕ accordingly. In summary, we apply $p_T > 1.92$ GeV for $|\phi_\gamma| > 35^\circ$ and $p_T > 5.65$ GeV for $|\phi_\gamma| \leq 35^\circ$, where p_T is in the coordinate system of the forward calorimeter BeamCal.

E Third, we require a minimum energy of the photon. The minimum energy of 2 GeV is applied to reject reconstructed photon candidates which might be the result of noise in the detector. In the earlier study [1], the maximum energy cut of 220 GeV was used to reduce contributions from Z return events.

82 We, however, no longer use the cut since we confirmed that the sensitivities for lower WIMP mass regions
83 do not change much even if we remove the cut.

84 **3.2 P_T cut for charged particles**

85 The electrons and positrons in Bhabha scattering events typically have higher energies than the charged
86 particles from beam-induced background. To reduce the background with keeping as many signal events
87 as possible, a tighter cut is necessary for electrons and positrons to suppress Bhabaha events while a
88 looser cut is more suitable for the other charged particles to save signal events with contamination from
89 beam-induced background. We applied the maximum P_T of 0.5 GeV for electrons and positrons and
90 3 GeV for the other charged particles.

91 **3.3 Visible E cut**

92 To check the overall detector activity in the surviving events after the p_T cut, we consider the energy sum
93 of charged and neutral particles excluding the signal photon. Here we summed the energies of particles
94 that passed a minimum energy cut of 5 GeV, because very soft particles could be created even in signal
95 events due to beam-induced background. It should be also noted that, even in the signal events, extra ISR
96 photons could create high-energetic neutrons by photonuclear reactions. Therefore we put relatively a
97 loose cut for events containing neutrons, while we put relatively a tight cut for events containing photons,
98 electrons, muons and V_0 particles to suppress SM processes effectively. We applied the maximum energy
99 sum cut of 30 GeV for all the particles excluding the signal photon and 10 GeV for all photons but the
100 signal photon, electrons, muons and V_0 particles.

101 **3.4 BCal veto**

102 We finally require no clusters in BCal, i.e. reconstructed objects clearly above the expected beam-induced
103 background, to suppress Bhabha scattering events with very forward leptons.

4 Performance of photon reconstruction and event selection

4.1 Photon reconstruction

We identified the event containing a single signal photon at least at generator information level so that we can assume a single signal photon should be reconstructed. For those MC signal events, the number of reconstructed photons is plotted as a function of the energy and the polar angle. Figure 2 shows two examples, which were produced with a IDR-S sample, $\nu\bar{\nu} + 1g$, eLpR case. In some cases, multiple hits created by a single photon are split into multiple ECal-clusters and accordingly are reconstructed as multiple photons. We found that the overall level of photon splitting is reasonably low (below 1%).

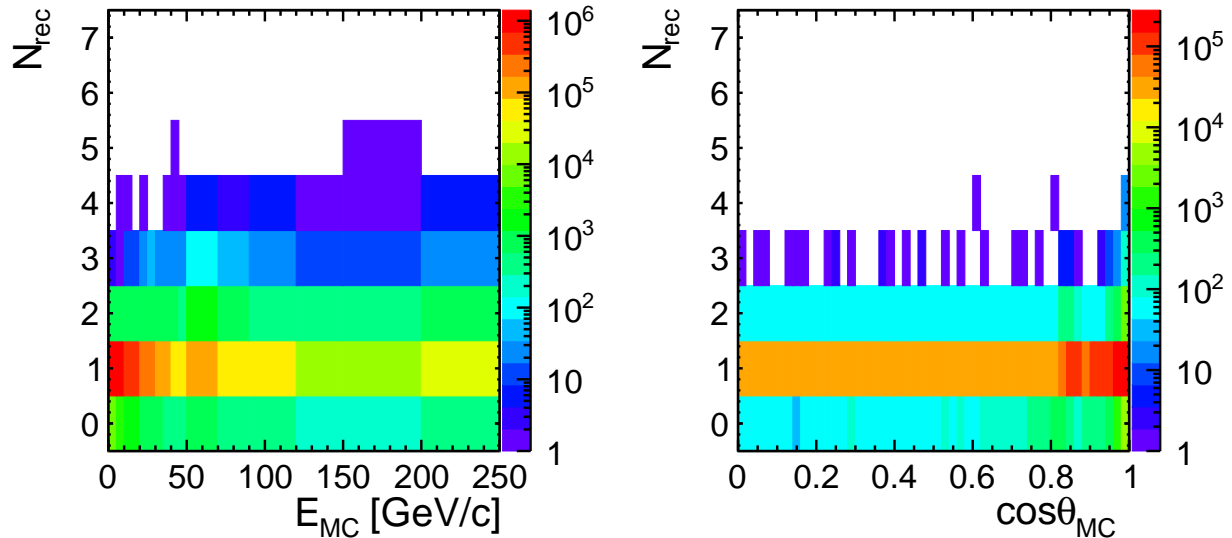


Figure 2: Number of reconstructed photons with regard to the energy of the MC photon in single photon events (left). Number of reconstructed photons with regard to the polar angle of the MC photon in single photon events (right).

Based on such 2D plots shown in Fig. 2, the averaged number of reconstructed photons and the RMS of the number of reconstructed photons were computed for each x-bin. The averaged number of reconstructed photons per generated photon ($N_{gen}=1$ for this performance study) is shown as a function of the energy and the polar angle in Fig. 3.

A clear drop can be seen around $\cos\theta_{MC} \approx 0.8$ in the right-hand side of Fig. 3. The direction of $\cos\theta \approx \pm 0.8$ corresponds to the transition region between the barrel and the end-caps of the ECal. The IDR-S model has a smaller tracker radius than the IDR-L and thus the transition region of the IDR-S is located at a slightly larger $\cos\theta$ than that of the IDR-L. In these regions, ECal clusters from a single photon can be easily split into the barrel and the end-cap and results in either reconstruction failures or reconstructing multiple photons. Figure 4 shows fractions of events with different number of reconstructed photons as a function of the polar angles. This indicates the failure rate of photon reconstruction ($N_{rec}=0$) at the transition region is, for some reason, slightly ($\sim 1\%$ level) higher in the IDR-S than the one in the IDR-L.

Figure 5 shows a similar plot to Fig. 3 but without requiring the reconstructed particles to be photons. The right plot indicates that the drop is mainly caused by photon mis-identification at the reconstruction. The energy dependence with requiring $\cos\theta_{MC} < 0.7$ and $\cos\theta_{MC} < 0.9$ is shown in Fig. 6, which almost reproduce Fig. 3. This means the features around $\cos\theta_{MC} = 0.8$ does not affect much to the energy dependence.

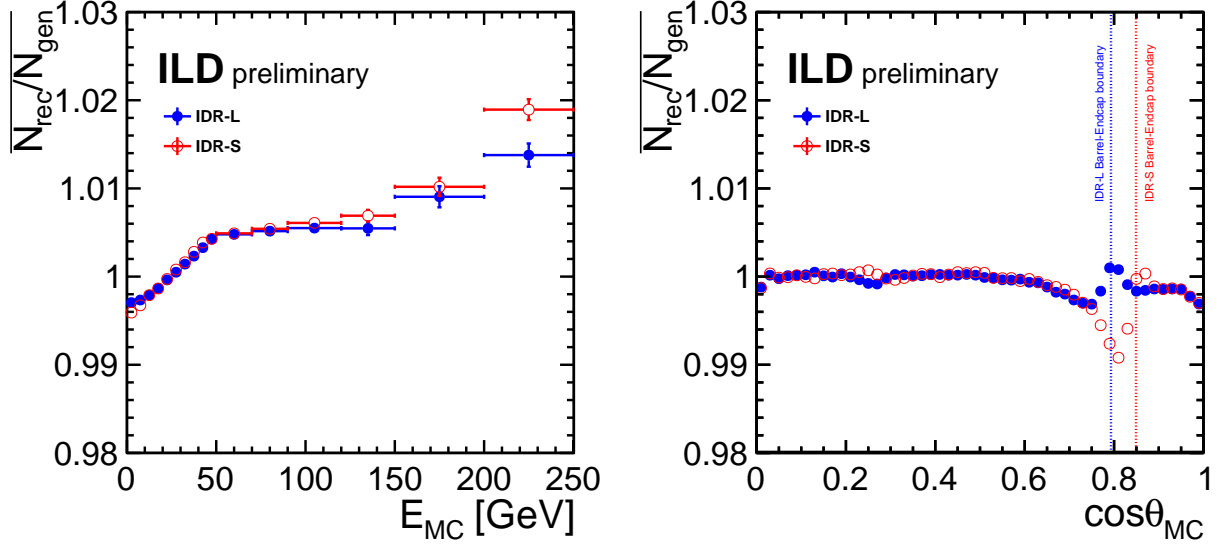


Figure 3: The number of reconstructed photons per generated photon as a function of the MC photon energy (left) and as a function of the polar angle of the MC photon (right).

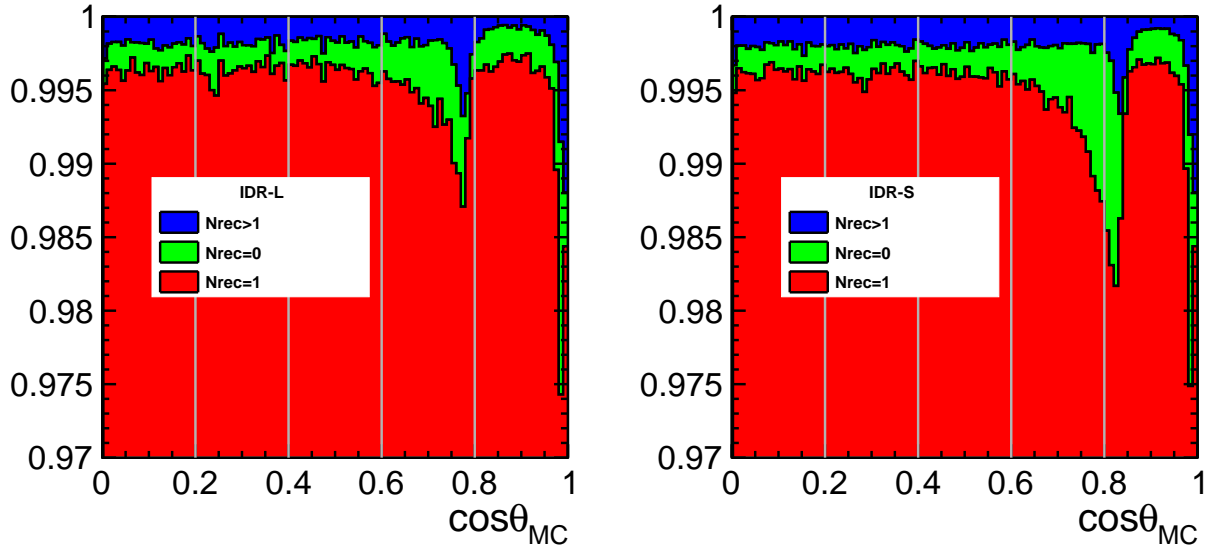


Figure 4: Fractions of events with different N_{rec} (number of reconstructed photons) as a function of the polar angles for IDR-L (left) and IDR-S (right). The larger fraction of the blue ($N_{rec} > 1$) corresponds to larger N_{rec}/N_{gen} in Fig. 3, while the larger fraction of the green ($N_{rec} = 0$) corresponds to smaller N_{rec}/N_{gen} .

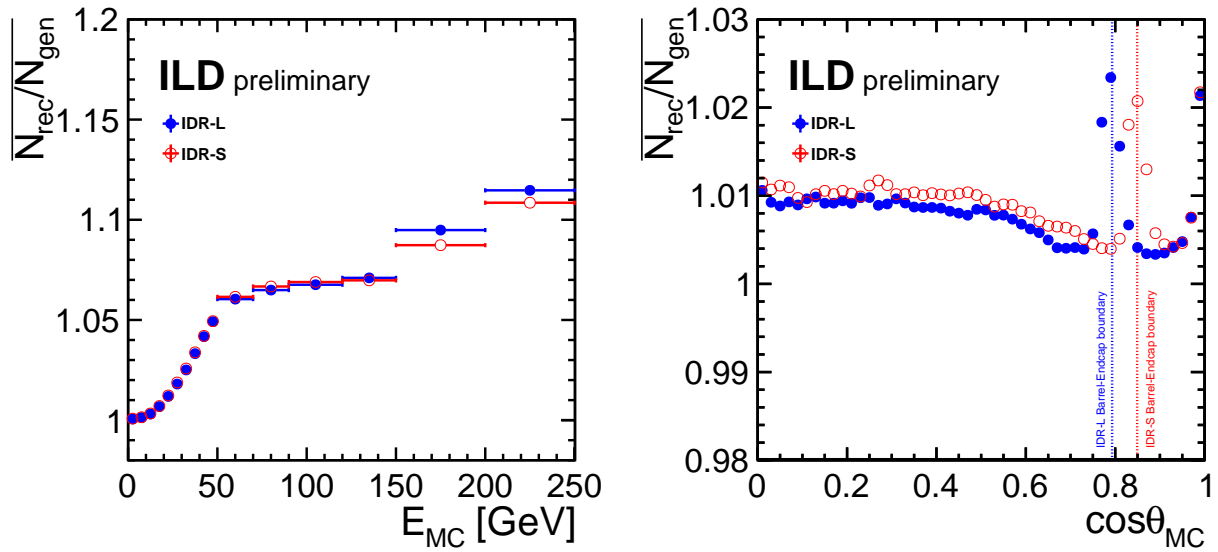


Figure 5: The number of reconstructed particles, which can be photon or anything else, per generated photon as a function of the MC photon energy (left) and as a function of the polar angle of the MC photon (right).

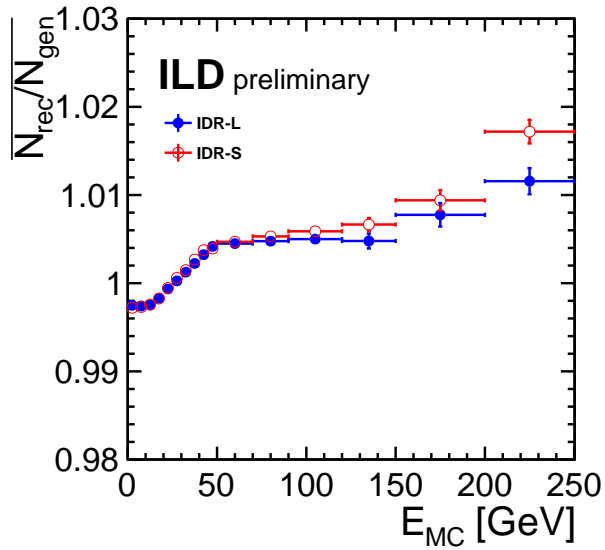


Figure 6: The number of reconstructed photons per generated photon with $j\cos\theta_{\text{MC}j} < 0.7$ or $j\cos\theta_{\text{MC}j} > 0.9$ as a function of the energy of the MC photon.

131

4.2 P_T distribution

132

133

134

135

136

137

138

Figure 7 shows the transverse momentum distribution of reconstructed electrons and positrons. The colors indicate different origins of the processes; particles that originate from overlay, daughter particles of a matrix element photon (i.e. photons which converted into a pair of charged particles) and the remaining particles. The Bhabha scattering events have more high-energetic charged particles than the neutrino pair production, which is regarded as the WIMP signals as well as the irreducible background in this analysis. This tells us that the transverse momentum cuts are suitable criteria to suppress the reducible background. Likewise, Fig. 8 shows the transverse momentum distribution of reconstructed charged PFOs.

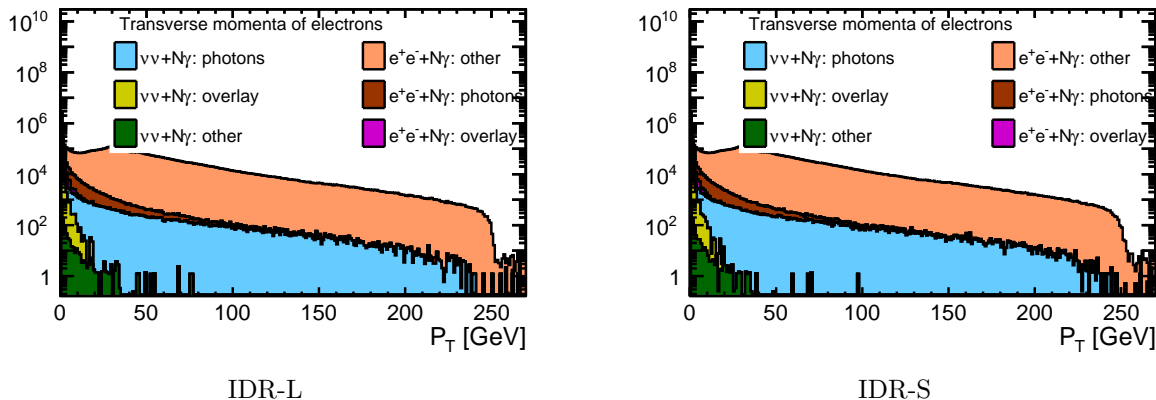


Figure 7: Comparison between IDR-L and IDR-S models on the transverse momentum of electrons and positrons in events that fulfill the signal selection described at Sec.3. An integrated luminosity of 500 fb^{-1} and no beam polarization are assumed. Events with a transverse momentum of an electron or positron above 0.5 GeV are discarded.

139

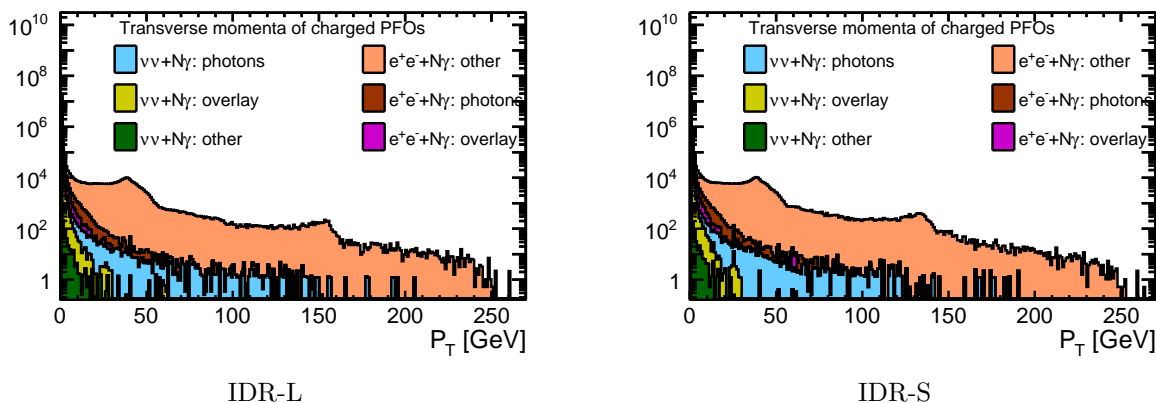


Figure 8: Same as Fig. 7 but on the transverse momentum of PFOs in events that fulfill the signal definition. Events with a charged p_T above 3 GeV are discarded. An integrated luminosity of 500 fb^{-1} and no beam polarization are assumed.

140

4.3 E distribution

141

142

Figures 9,10,11 show the energy distributions for neutral particles after the P_T cut. Figures 12,13,14 show the energy distributions for electrons, muons and pions, respectively. We did not apply any cuts for these

143
144
145
146
147

distributions, while we did for two types of energy sums in each event. The first one is the energy sum of all particles excluding the signal-like photon and the particle whose energy is less than 5 GeV as shown in Fig. 15. We require this energy sum to be below 30 GeV for signal events. The second energy sum is the same as the first one except for excluding neutrons and pions and we required less than 10 GeV as shown in Fig. 16.

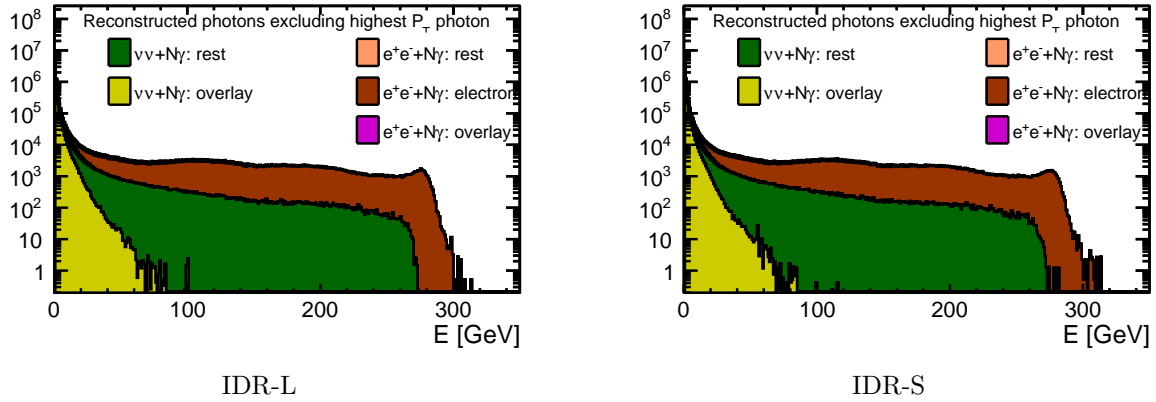


Figure 9: Energy of photons in the remaining events after the p_T cuts, assuming an integrated luminosity of 500 fb^{-1} and no beam polarization.

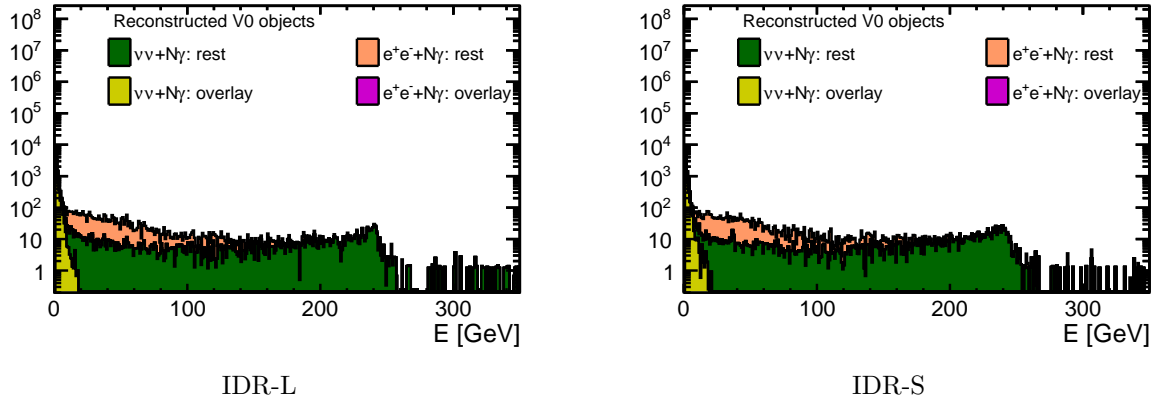


Figure 10: Energy of V0s in the remaining events after the p_T cuts. An integrated luminosity of 500 fb^{-1} and no beam polarization are assumed.

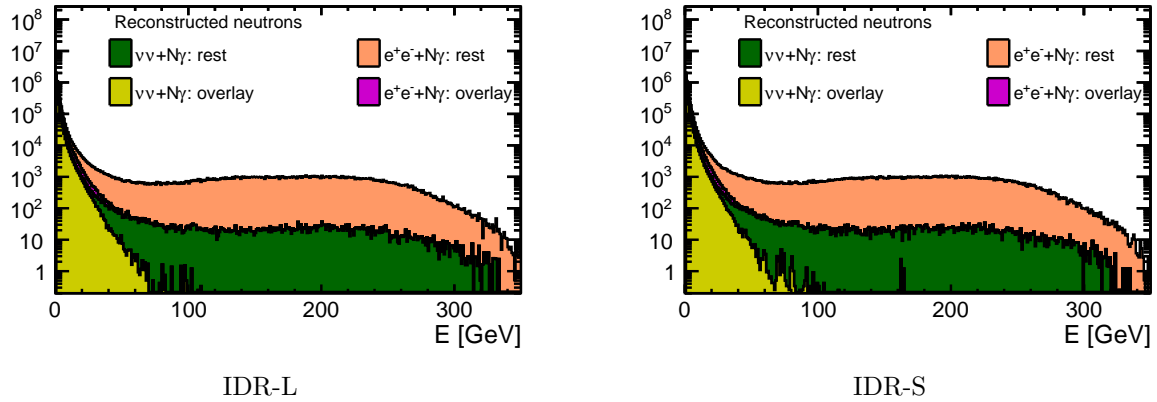


Figure 11: Energy of neutrons in the remaining events after the p_T cuts, assuming an integrated luminosity of 500 fb^{-1} and no beam polarization.

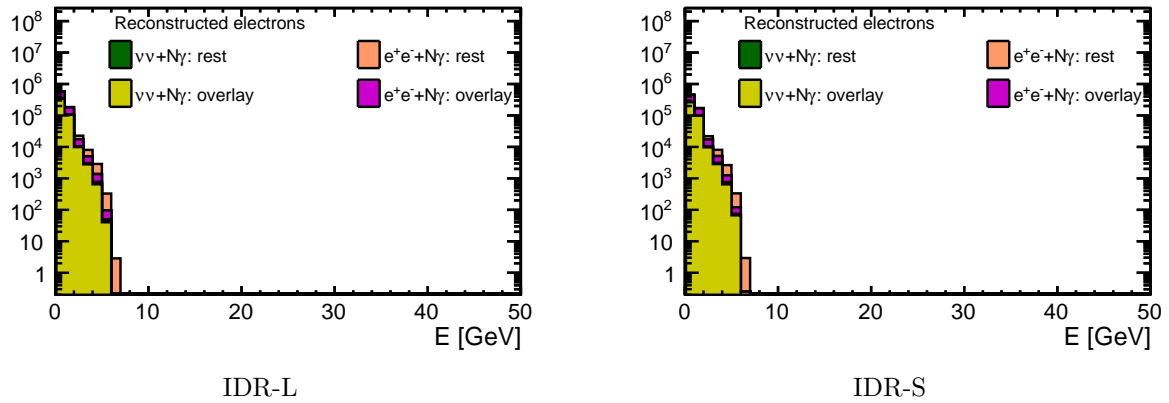


Figure 12: Energy of electrons in the remaining events after the p_T cuts. Due to the previous cuts on the transverse momentum of charged particles, the energy range of the remaining electrons is restricted to lower values and originate mainly from overlay. An integrated luminosity of 500 fb^{-1} and no beam polarization are assumed.

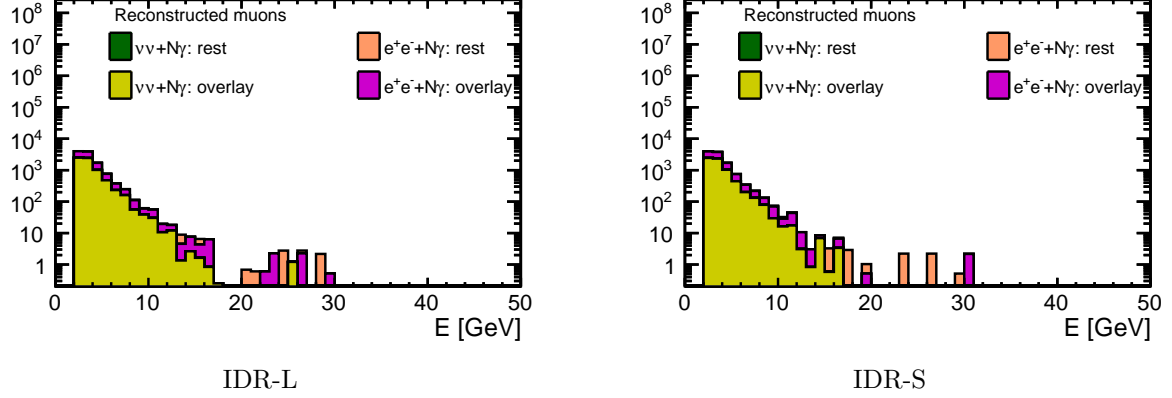


Figure 13: Energy of muons in the remaining events after the p_T cuts. Due to the previous cuts on the transverse momentum of charged particles, the energy range of the remaining muons is restricted to lower values and originate mainly from overlay. An integrated luminosity of 500 fb^{-1} and no beam polarization are assumed.

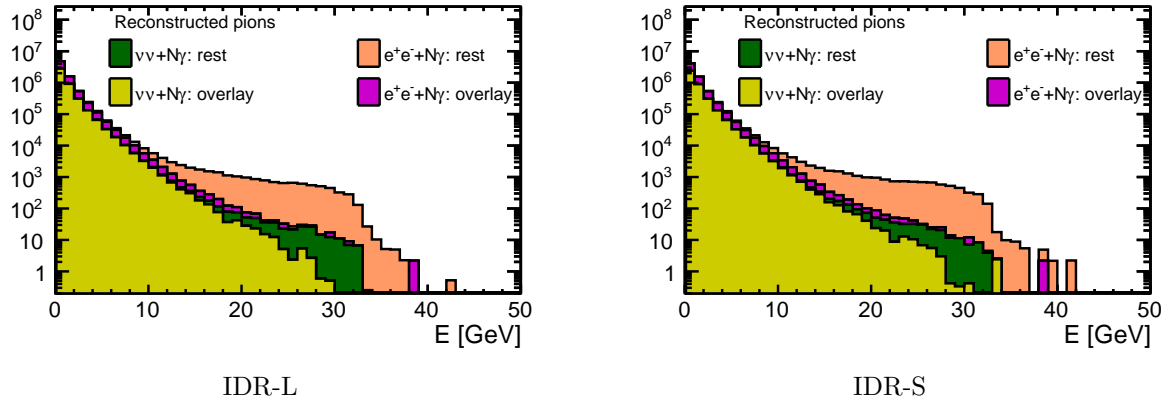


Figure 14: Energy of pions in the remaining events after the p_T cuts. Due to the previous cuts on the transverse momentum of charged particles, the energy range of the remaining pions is restricted to lower values and originate mainly from overlay. An integrated luminosity of 500 fb^{-1} and no beam polarization are assumed.

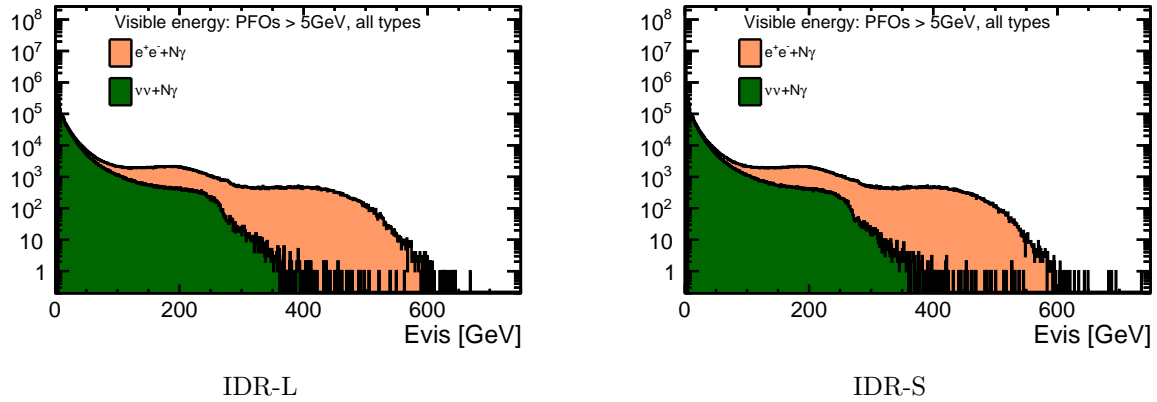


Figure 15: Sum of the energies of all PFOs in the event, without the signal photon. Events remaining after the p_T criterion are considered. An integrated luminosity of 500 fb^{-1} and no beam polarization are assumed.

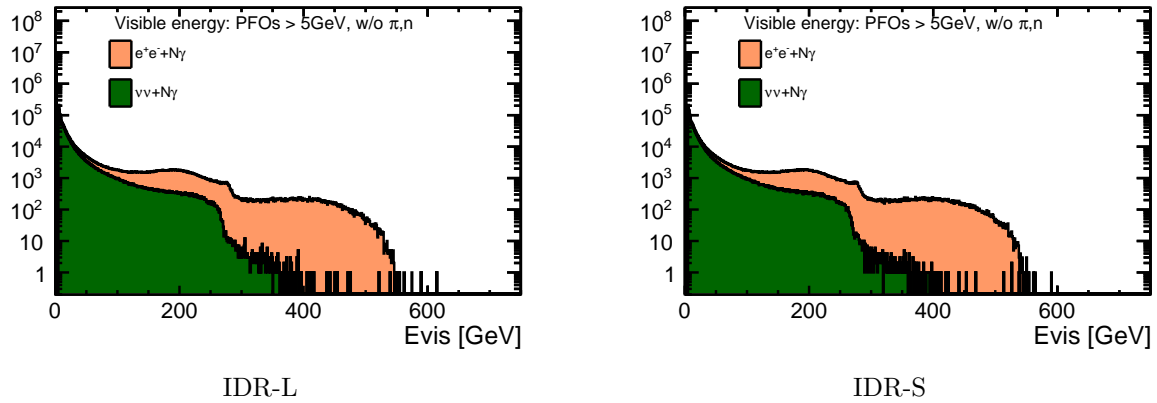


Figure 16: Sum of the energies of PFOs except for neutrons and pions in the event, without the signal photon. Events remaining after the p_T criterion are considered. An integrated luminosity of 500 fb^{-1} and no beam polarization are assumed.

148

4.4 BeamCal veto

149

150

151

152

153

154

155

Figures 17 show the number of clusters in BeamCal. In the signal events, we expect no clusters in BeamCal except for contributions from beam-induced background. On the other hand, SM background including Bhabha scattering process is expected to have more activity in the BeamCal and thus BeamCal vetoing plays an important role in this analysis.

Figures 18 show same data as Fig. 17 but in a different way. The canvases correspond to $\nu\nu + 1\gamma$, $\nu\nu + N\gamma$ and $e^+e^- + N\gamma$ respectively, and the histograms for IDR-L and IDR-S are shown together. The difference between IDR-L and IDR-S turned out to be negligible.

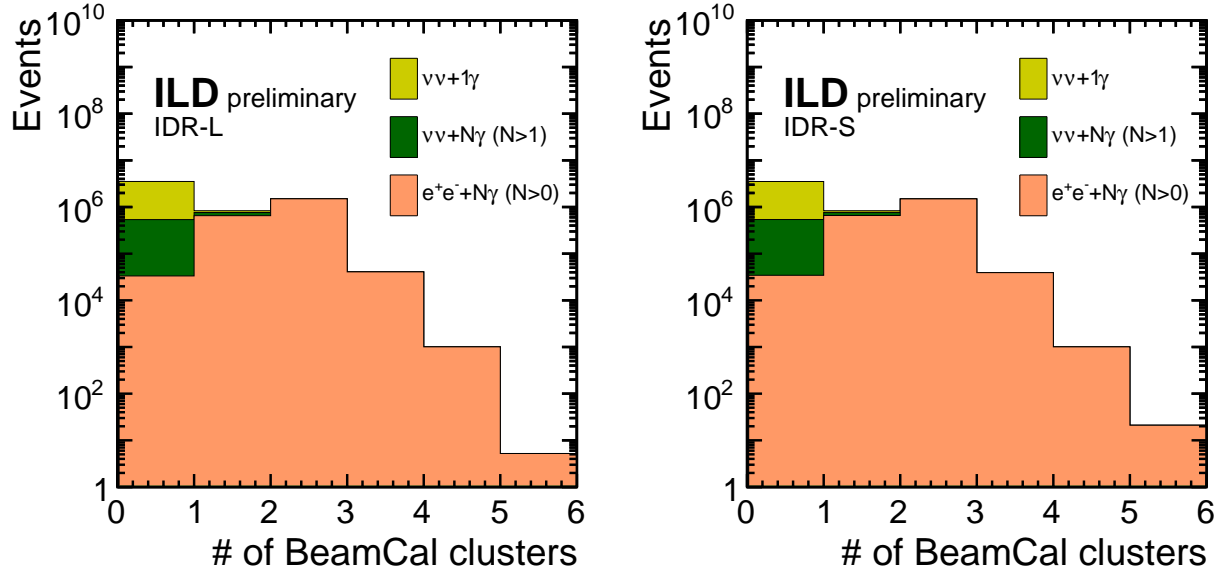


Figure 17: Comparison between IDR-L and IDR-S models on the number of BCal clusters, obtained assuming an integrated luminosity of 500 fb^{-1} and no beam polarization. The histograms are stacked.

156

4.5 Reduction summary

157

Table 3 shows how the number of events for each process are reduced by the criteria mentioned above.

Model	process	(e^- pol., e^+ pol.)	No cut	Sig. sel.	Pt cut	E cut	BCal veto	Efficiency
IDR-L	$\nu\nu N\gamma$	(-1,+1)	16719834	10778958	9539097	8729764	8412417	78.04%
		(+1,-1)	1158368	808799	706732	609899	570408	70.53%
	$eeN\gamma$	(-1,-1)	2966600	961712	221701	106540	1555	0.16%
		(-1,+1)	2937200	1024991	206525	98850	1496	0.15%
		(+1,-1)	2995400	1021891	214584	102685	1572	0.15%
		(+1,+1)	2993200	970348	222783	107293	1586	0.16%
IDR-S	$\nu\nu N\gamma$	(-1,+1)	16854834	10853639	9589298	8776125	8469617	78.03%
		(+1,-1)	1162568	809934	706858	609975	571393	70.55%
	$eeN\gamma$	(-1,-1)	2999800	971815	223708	107994	1690	0.17%
		(-1,+1)	2990600	1043084	209579	100432	1542	0.15%
		(+1,-1)	2999600	1023152	215019	102725	1596	0.16%
		(+1,+1)	2999800	971359	222723	107123	1642	0.17%

Table 3: The number of events passed through each cut. The last column shows remaining fractions from the signal selection step (“Sig. sel.”).

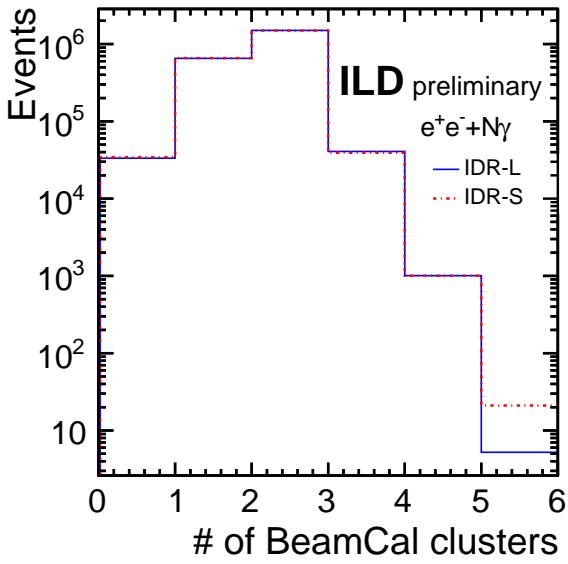
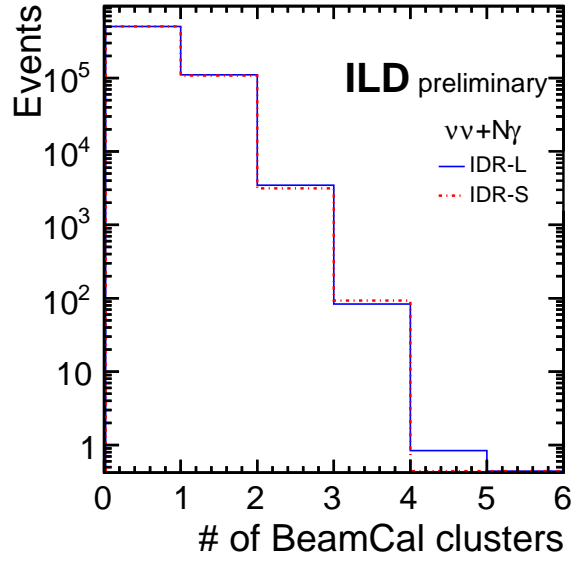
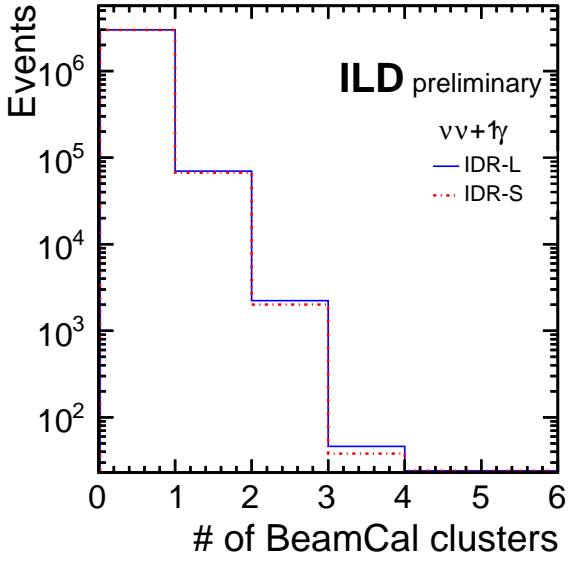


Figure 18: Comparison of the number of BeamCal clusters between IDR-L and IDR-S models in each process.

5 Physics performance

The H20 scenario is one of the ILC running scenarios considered to investigate the ultimate physics reach of the ILC in terms of energy stages, integrated luminosities, and polarization sharing [9]. Table 4 summarizes the sharing of the integrated luminosity for the H20 scenario : 1600 fb⁻¹ each with the opposite sign polarization combinations $P(e^-, e^+) = (\pm 80\%, \mp 30\%)$ and 400 fb⁻¹ each for the same sign combinations ($\pm 80\%, \pm 30\%$) at $\sqrt{s} = 500$ GeV.

Figure 19 shows the exclusion limits for different effective operators in the case of the H20 scenario. The testable energy scales are in the range of $\Lambda = 2.6 \sim 3.1$ TeV. It shows we can test WIMP masses up to almost the reachable kinematic limit, and down to 1 eV. No difference between IDR-L and IDR-S was observed. For technical details, see Chapter 7 in [1] and in particular Sec 7.4 for systematic uncertainties considered here.

beam polarization (P_{e^-}, P_{e^+})	(-80%,-30%)	(-80%,+30%)	(+80%,-30%)	(+80%,+30%)
Integrated Luminosity [fb ⁻¹]	400	1600	1600	400

Table 4: Luminosity sharing for $\rho_{\bar{s}} = 500$ GeV in H20 scenario.

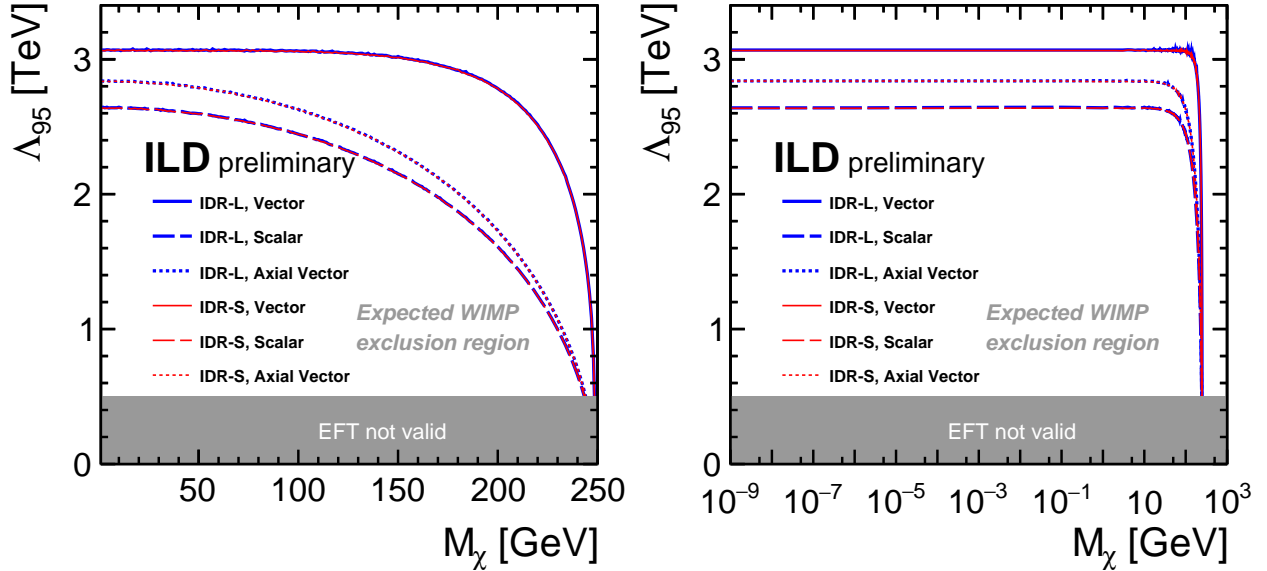


Figure 19: 95% confidence level exclusion limits for different effective operators with a realistic sharing of the polarization at 4ab⁻¹ of H20 scenario at $\rho_{\bar{s}} = 500$ GeV. Left:x-range[1,250], Right:x-range[10⁻⁹ : 10³].

6 Conclusion

We examined the detector and physics performances for two different ILD detector models namely IDR-L and IDR-S. Both IDR-L and IDR-S offer excellent photon reconstruction performance. We found 1% level degradation of photon identification around the barrel-endcap boundary in IDR-S, which may require an optimization of PandoraPFA parameters dedicated to IDR-S. We found almost identical physics performance between IDR-L and IDR-S and both of them meet the key requirements in this WIMP search.

Acknowledgement

The author would like to thank the LCC generator working group and the ILD software working group for providing the simulation and reconstruction tools and producing the Monte Carlo samples used in this study, and acknowledges the dedicated helps of Dr. Moritz Habermehl and Dr. Aleksander Filip Źarnecki to prepare this document. This work has benefited from computing services provided by the ILC Virtual Organization, supported by the national resource providers of the EGI Federation and the Open Science GRID. We thank our ILD colleagues for helpful discussions on the analysis.

References

- [1] Moritz Habermehl. *Dark Matter at the International Linear Collider*. PhD thesis, DESY, Hamburg, 2018.
- [2] https://github.com/ILDAnaSoft/ILDbench_WIMP.
- [3] Christoph Bartels, Mikael Berggren, and Jenny List. Characterising WIMPs at a future e^+e^- Linear Collider. *Eur. Phys. J.*, C72:2213, 2012.
- [4] Christoph Bartels. *WIMP Search and a Cherenkov Detector Prototype for ILC Polarimetry*. PhD thesis, DESY, Hamburg, 2011.
- [5] Wolfgang Kilian, Thorsten Ohl, and Jurgen Reuter. WHIZARD: Simulating Multi-Particle Processes at LHC and ILC. *Eur. Phys. J.*, C71:1742, 2011.
- [6] Mauro Moretti, Thorsten Ohl, and Jurgen Reuter. O’Mega: An Optimizing matrix element generator. pages 1981–2009, 2001.
- [7] Markus Frank, F. Gaede, C. Grefe, and P. Mato. DD4hep: A Detector Description Toolkit for High Energy Physics Experiments. *J. Phys. Conf. Ser.*, 513:022010, 2014.
- [8] https://ilcsoft.desy.de/MarlinReco/current/doc/manual_html/manual.html.
- [9] T. Barklow, J. Brau, K. Fujii, J. Gao, J. List, N. Walker, and K. Yokoya. ILC Operating Scenarios. 2015.